

Figure 2.13 The best fit spectral models for the time-resolved spectra of four bright GRBs detected by *Fermi* GBM and LAT. *First row:* GRB 080916C. From Abdo et al. (2009c). *Second row:* GRB 090902B. Reproduced from Figure 3 in Abdo et al. (2009b) with permission. ©AAS. *Lower left:* Short GRB 090510. Reproduced from Figure 5 in Ackermann et al. (2010) with permission. ©AAS. *Lower right:* GRB090926. Reproduced from Figure 5 in Ackermann et al. (2011) with permission. ©AAS.

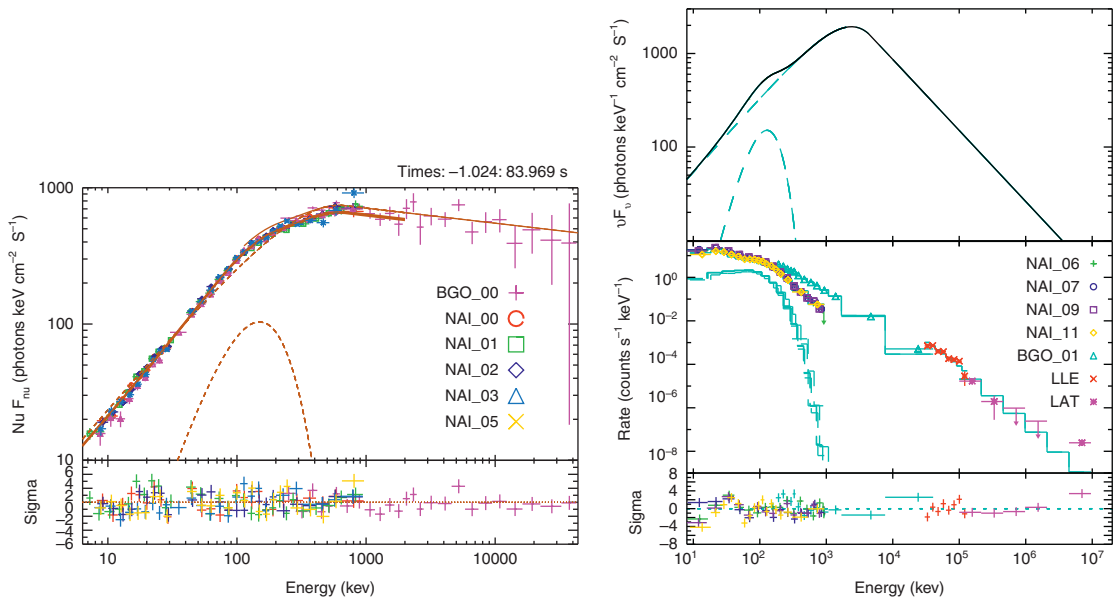


Figure 2.15 Spectral fits and residuals to the time-integrated spectra of two GRBs that show superposition of a thermal (blackbody) component on a non-thermal (Band) component. *Left:* GRB 100724B. Reproduced from Figure 2 in Guiriec et al. (2011) with permission. ©AAS. *Right:* GRB 110721A. Reproduced from Figure 2 in Axelsson et al. (2012) with permission. ©AAS.

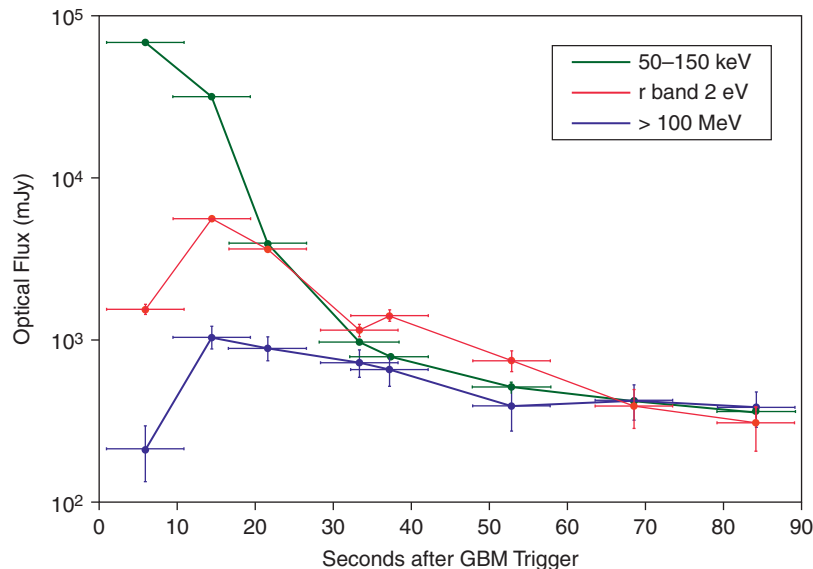


Figure 2.18 Multi-wavelength lightcurves of the nearby bright GRB 130427A, which show a coincident optical and GeV flash. From Vestrand et al. (2014).

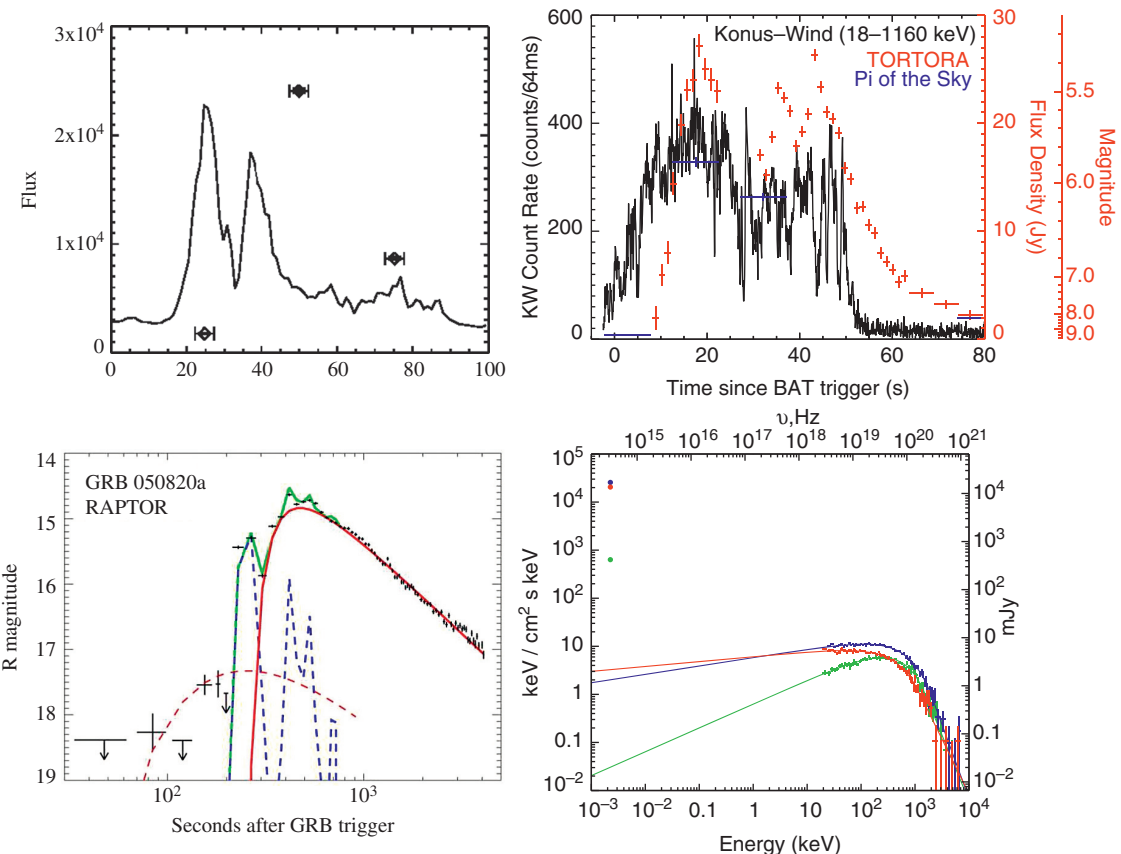


Figure 2.19

Examples of prompt optical emission that show three patterns with respect to the γ -ray emission. *Top left:* GRB 990123 shows an offset of optical peak with respect to the γ -ray emission peak. From Akerlof et al. (1999). *Top right:* GRB 080319B (the “naked-eye” GRB) shows a clear tracking behavior between optical and γ -rays. From Racusin et al. (2008). *Lower left:* GRB 050820A shows the “hybrid” pattern. From Vestrand et al. (2006). *Lower right:* The optical emission of the naked-eye GRB has a distinct spectral component from the γ -rays. From Racusin et al. (2008). The three dots in the optical band (upper left region in the plot) from top to bottom are related to the three curves in the γ -ray band, respectively, with the same top-to-bottom order in terms of the peak flux of the curves.

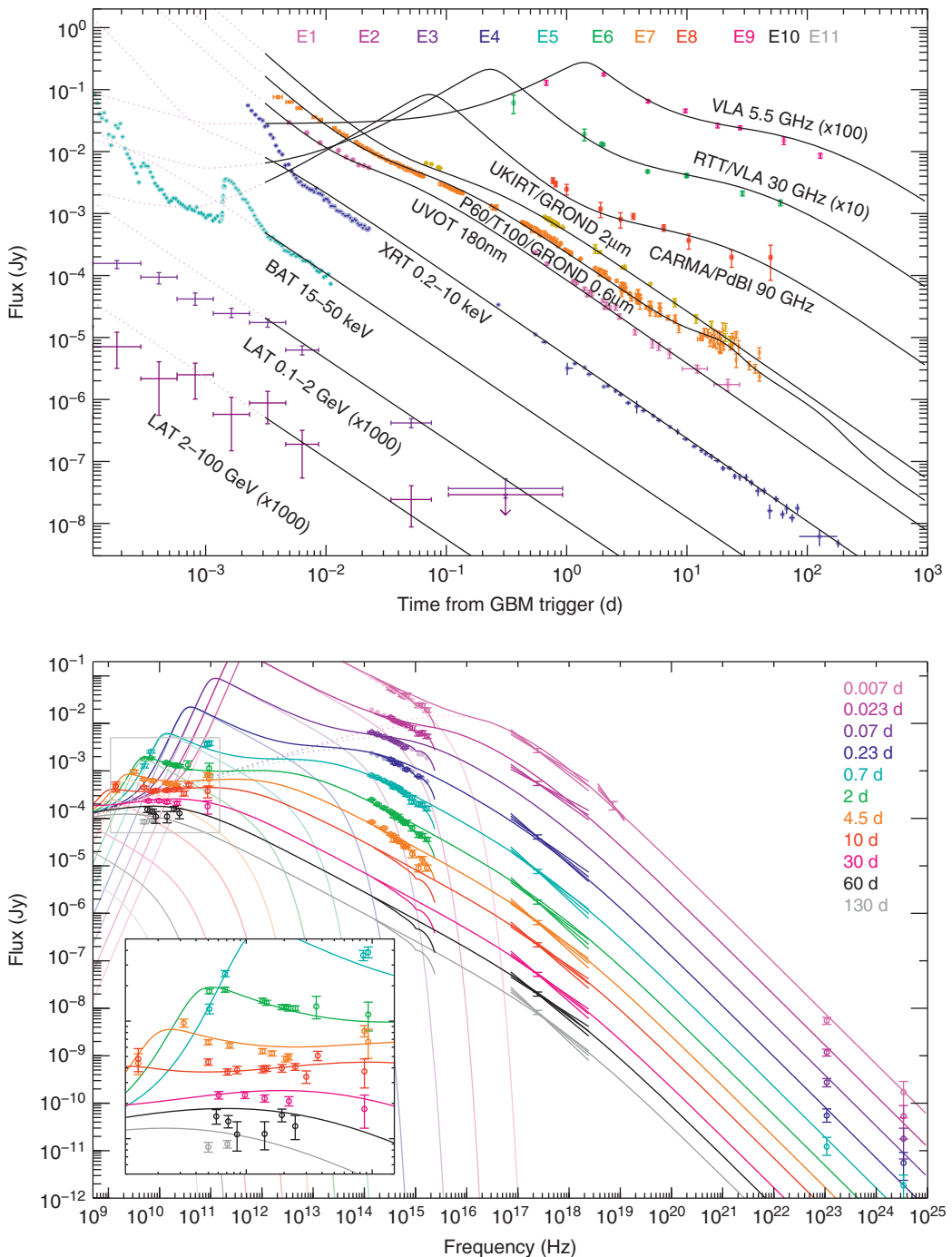


Figure 2.20 Multi-wavelength afterglow lightcurves (*upper panel*) and multi-epoch spectral energy distributions (*lower panel*) of GRB 130427A. Reproduced from Figures 10 and 11 in Perley et al. (2014) with permission. ©AAS.

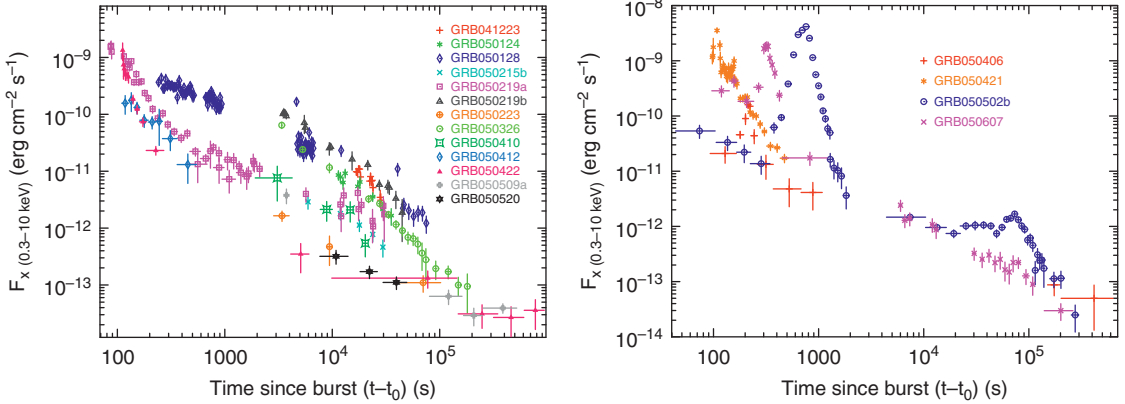


Figure 2.21 Some examples of X-ray afterglow lightcurves detected with *Swift* XRT. Reproduced from Figure 2 in Nousek et al. (2006) with permission. ©AAS.

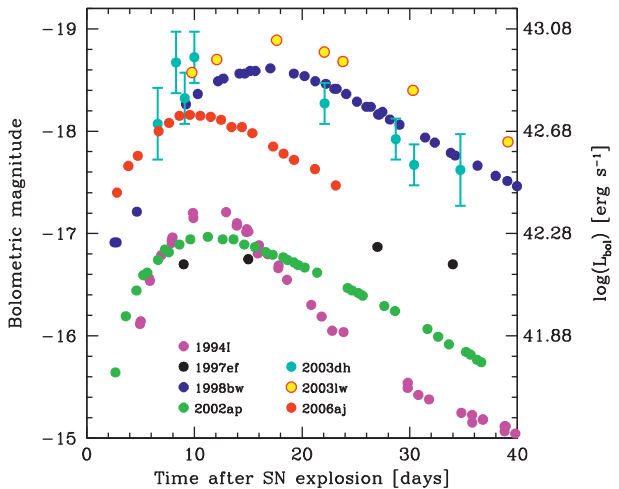


Figure 2.36 Lightcurves of several GRB-associated Type Ic SNe (1998bw, 2003dh, 2003lw, 2006aj) compared with other Type Ic SNe (1994I, 1997ef, 2002ap). From Pian et al. (2006).

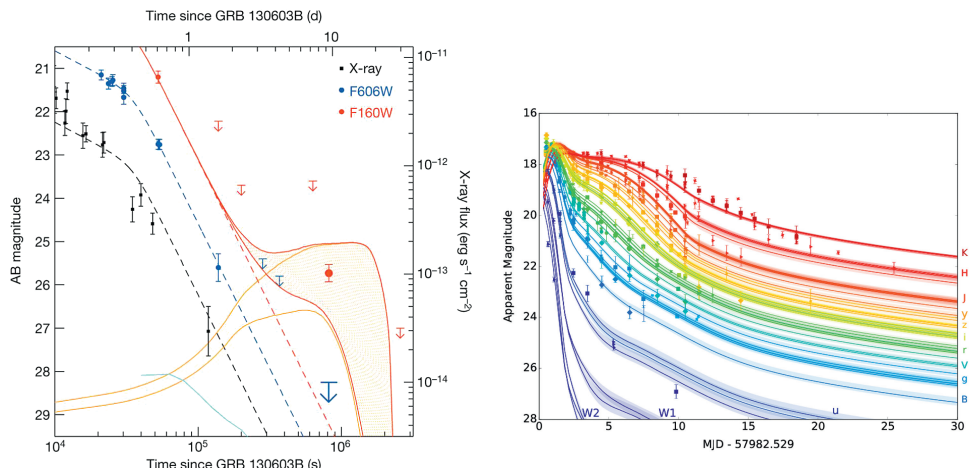


Figure 2.38 *Left:* Multi-wavelength lightcurves of GRB 130603B showing an IR excess that is consistent with a “kilonova”. From Tanvir et al. (2013). *Right:* Broad-band lightcurves of GW170817 showing a clear signature of a macronova/kilonova. Reproduced from Figure 1 in Villar et al. (2017) with permission. ©AAS.

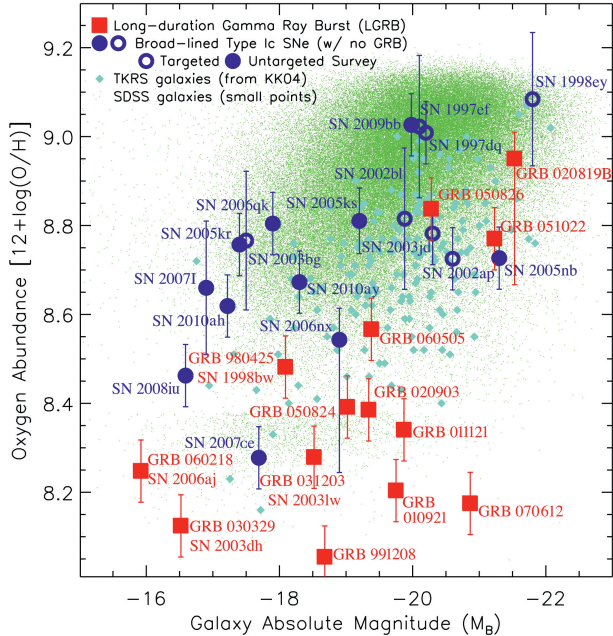


Figure 2.39 A comparison of metallicity of long GRB host galaxies with the host galaxies of other broad-line Type Ic SNe not associated with GRBs, Type II SNe, as well as the Sloan Digital Sky Survey galaxy sample. Long GRB hosts on average tend to be more metal poor than other samples. Reproduced from Figure 3 in Graham and Fruchter (2013) with permission. ©AAS.

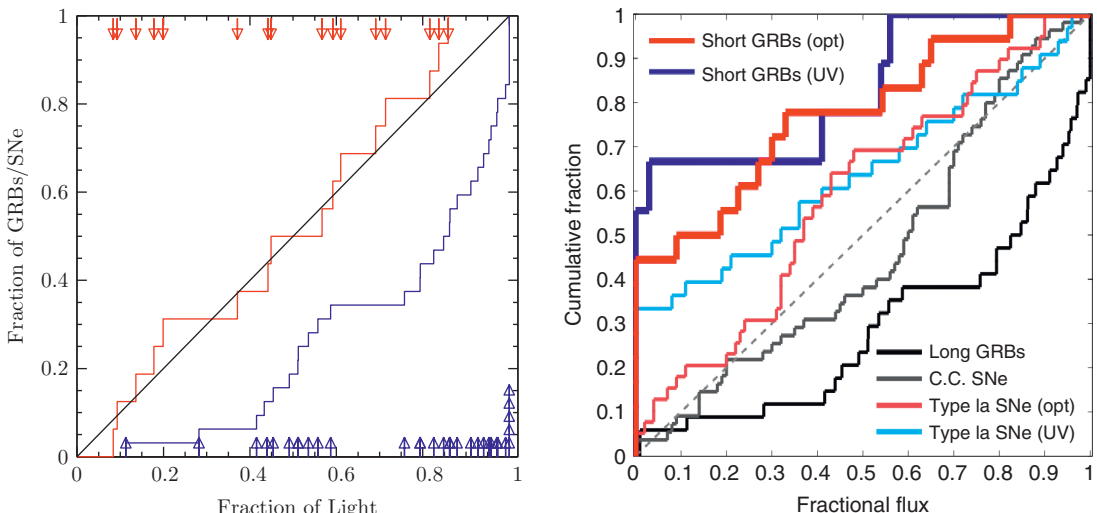


Figure 2.40 *Left:* A comparison between the locations of long GRBs and core-collapse SNe in their host galaxies. From Fruchter et al. (2006). *Right:* A more extended study also including short GRBs and Type Ia SNe. Reproduced from Figure 7 in Fong and Berger (2013) with permission. ©AAS.

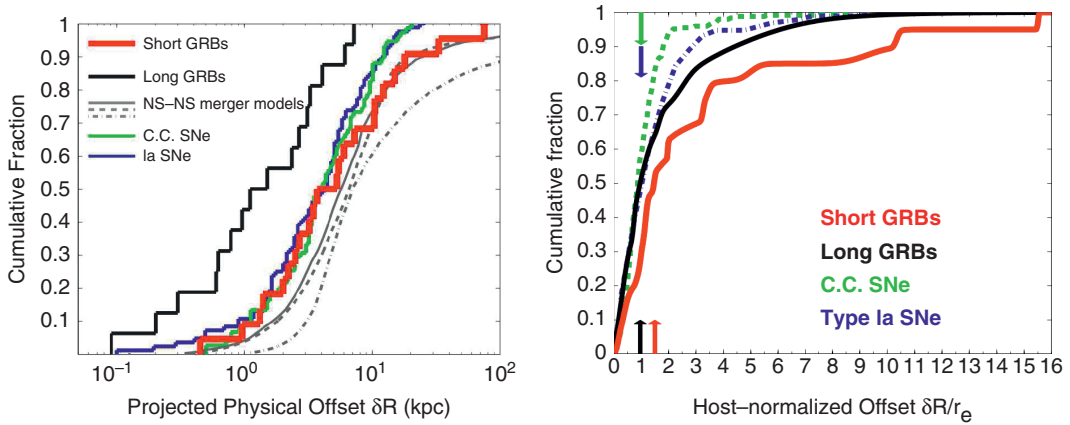


Figure 2.41 Projected physical and normalized offsets of short GRBs with respect to the center of their host galaxies, as compared with the offsets of other transients. Reproduced from Figures 5 and 6 in Fong and Berger (2013) with permission. ©AAS.

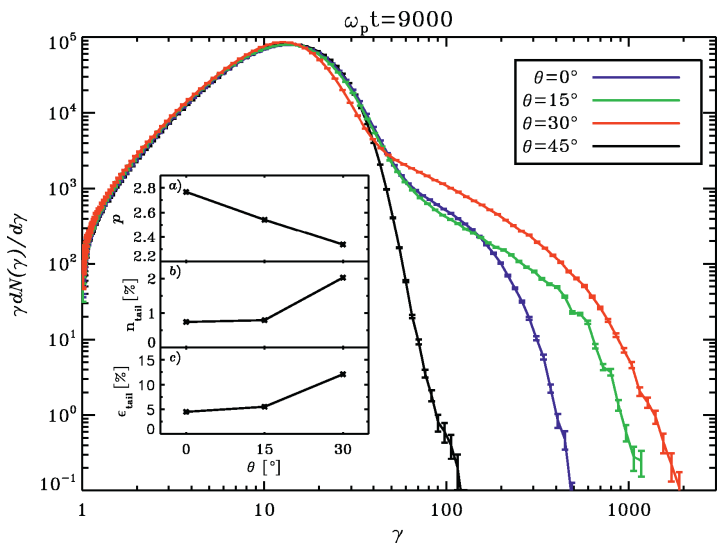


Figure 4.5 Particle-in-cell (PIC) simulations for magnetized pair shocks. The dependence of acceleration on the oblique angle of the magnetic field with respect to the shock normal was investigated. Reproduced from Figure 11 in Sironi and Spitkovsky (2009a) with permission. ©AAS.

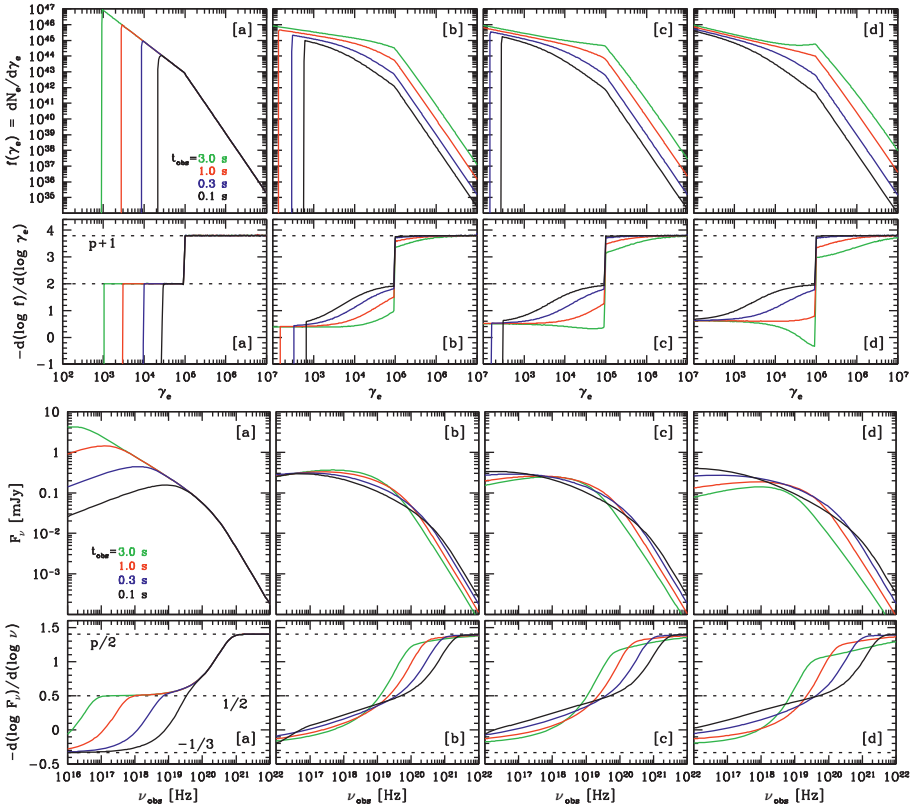


Figure 5.3 Fast cooling electron spectra (upper panel) and synchrotron photon spectra (lower panel) in a decaying magnetic field. Models [a], [b], [c], [d] have $b = 0, 1, 1.2, 1.5$, respectively. Other model parameters: $\gamma_m = 10^5$, Lorentz factor $\Gamma = 300$, comoving-frame magnetic field strength $B'_0 = 30$ G, $r_0 = 10^{15}$ cm, $p = 2.8$, and the injection rate $R_{\text{inj}} = \int_{\gamma_m}^{\infty} Q(\gamma_e, t') d\gamma_e = 10^{47} \text{ s}^{-1}$. From Uhm and Zhang (2014b).

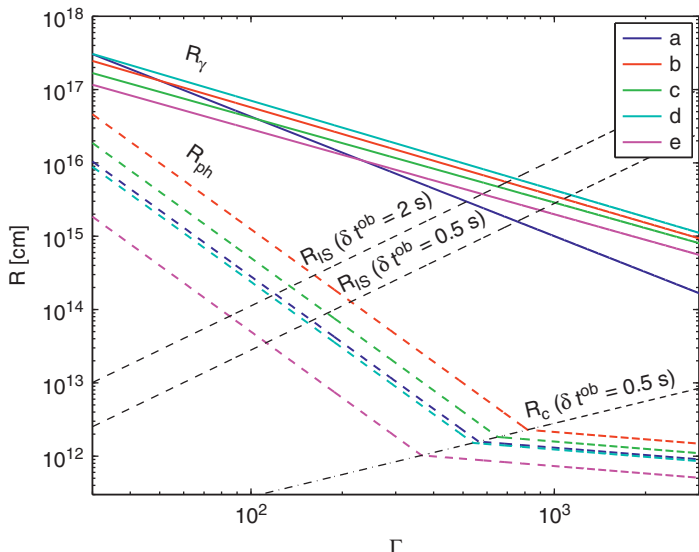


Figure 7.2 Constraints on Γ and R_γ (solid lines) based on the observational data of GRB 080916C (Abdo et al., 2009c). Different solid lines are derived using the highest photon energy $\epsilon_{\gamma,\text{max}}$ measured in different time intervals (a, b, c, d, and e) defined in Abdo et al. (2009c). Two parallel thin dashed lines denote the internal shock model with two assumed variability time scales. The thick dashed lines are the photosphere radius as a function of Γ for different time intervals. From Zhang and Pe'er (2009).

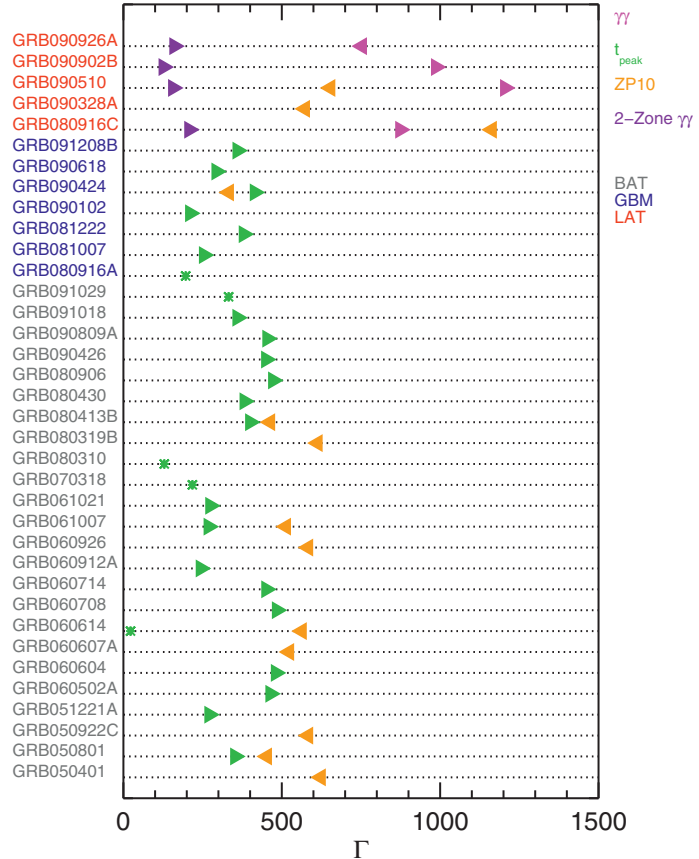


Figure 7.3 The constrained Lorentz factors of GRBs using various methods. From Racusin et al. (2011).

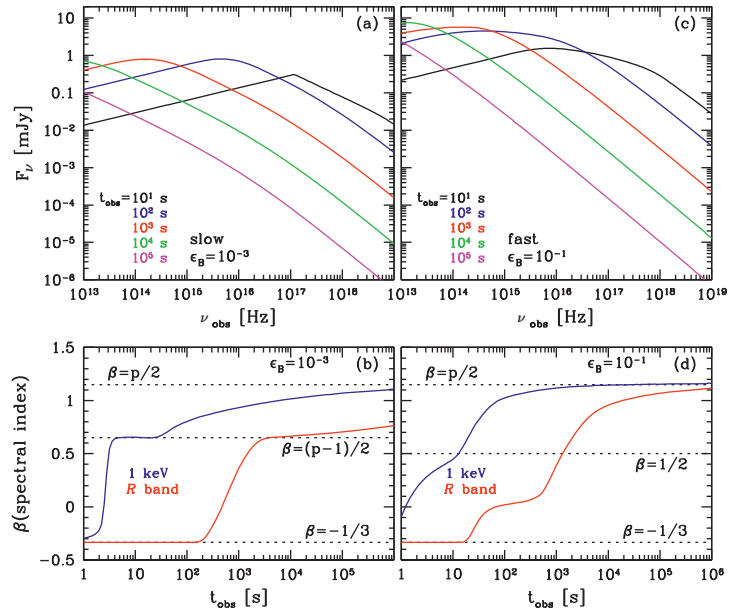


Figure 8.3 Detailed afterglow modeling that shows smooth breaks. The lower panel shows that it takes longer for the spectral indices to approach the analytical asymptotic values. From Uhm and Zhang (2014c).

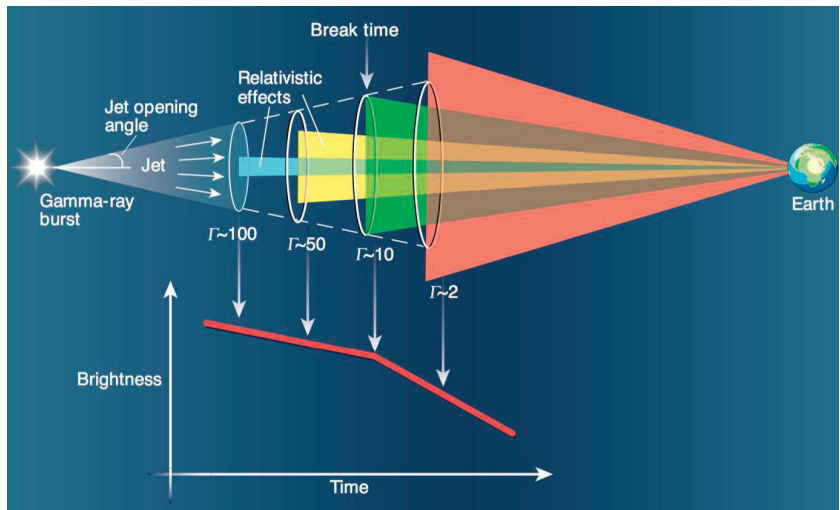


Figure 8.5 A cartoon picture for the jet break due to the edge effect. Since only those fluid elements whose Earth viewing direction is within the $(1/\Gamma)$ cone of direction of motion can give bright emission to Earth, the outer cross sections of the colored (blue, yellow, green, and orange) cones centered on Earth show the emission regions inside the jet where emission contributes to the observed flux. When the $1/\Gamma$ cone is greater than the jet opening angle θ_j (the orange cone), the observer feels a deficit of the flux, and hence the lightcurve shows a steepening break. From Woosley (2001).

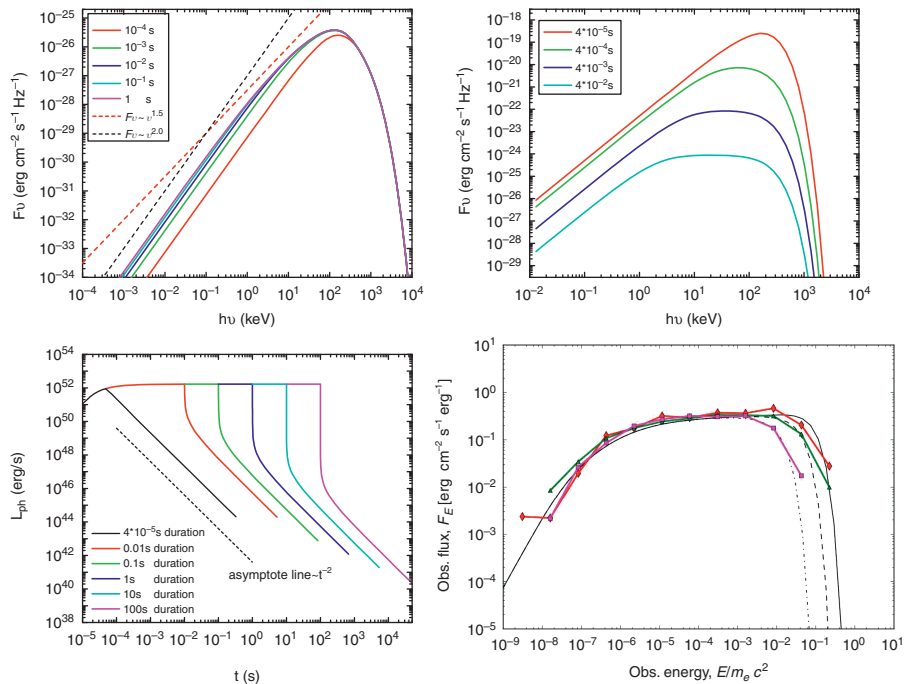


Figure 9.4 The predicted observational spectra of a non-dissipative photosphere. *Upper left:* Instantaneous spectra of a constant luminosity continuous wind. *Upper right:* The high-latitude-emission-dominated photosphere emission that shows a flat spectrum. *Lower left:* The lightcurve of photosphere emission for high-latitude emission, showing the abrupt drop followed by a t^{-2} decay. *Lower right:* An example spectrum for a special type of structured jet that reproduces a flat spectrum corresponding to $\alpha \sim -1$. First three panels from Deng and Zhang (2014b), last panel from Lundman et al. (2013).

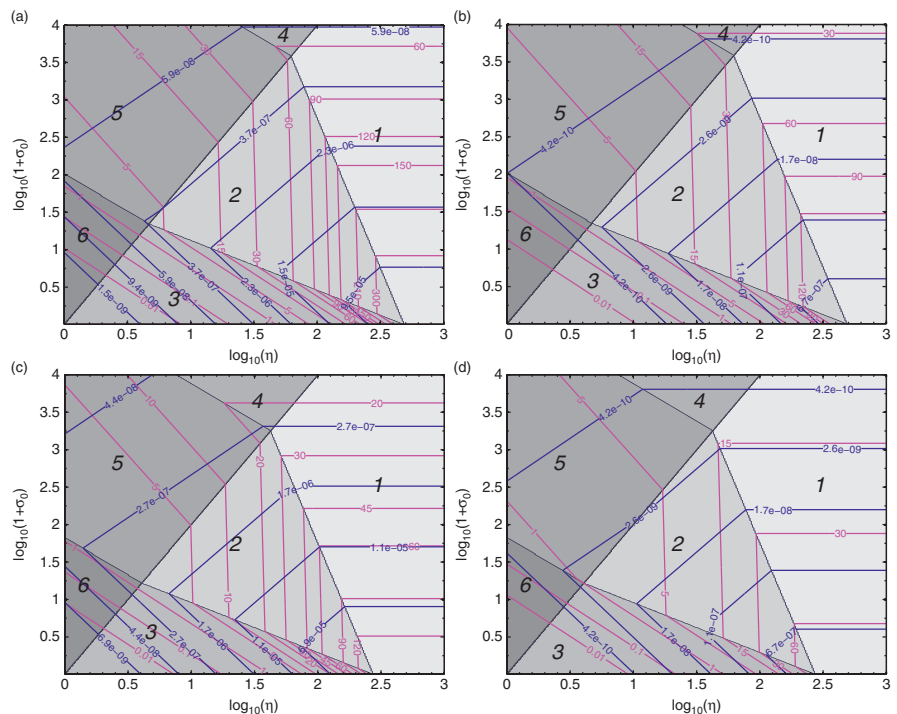


Figure 9.6

The temperature (in units of keV) and flux (in units of $\text{erg cm}^{-2} \text{s}^{-1}$) in the $(\eta, (1 + \sigma_0))$ domain. Parameters: $L_w = 10^{52} \text{ erg s}^{-1}$, $R_0 = 10^8 \text{ cm}$ (upper panels) or $R_0 = 10^9 \text{ cm}$ (lower panels), and $z = 0.1$ (left panels) or $z = 1$ (right panels). By measuring T_{ob} and F_{BB} , one can find a solution of $(\eta, (1 + \sigma_0))$ by assuming a R_0 value. From Gao and Zhang (2015).

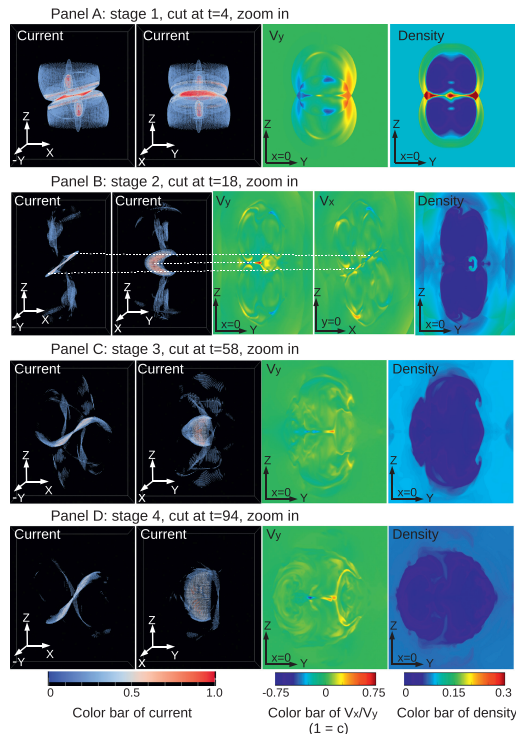


Figure 9.15

Numerical simulation results of ICMART events. Representative cuts of current, velocity, and density of four different stages (as defined in the upper panel) during one ICMART event, showing collision-triggered reconnection of high- σ blobs. From Deng et al. (2015).

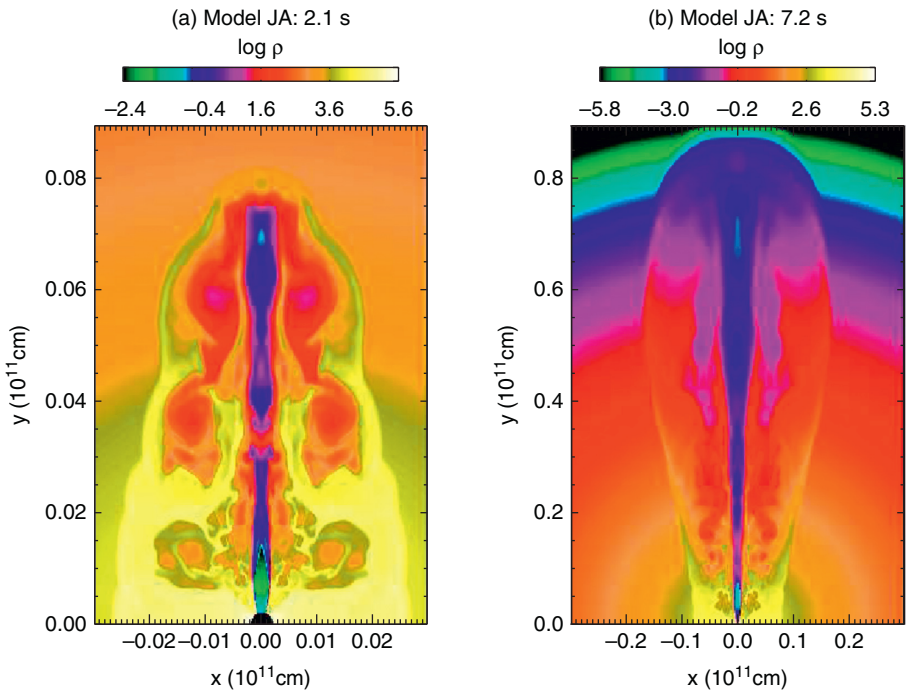


Figure 10.1 The jet–cocoon structure formed during the jet–envelope interaction. Numerical results. Reproduced from Figure 1 in Zhang et al. (2003b) with permission. ©AAS.

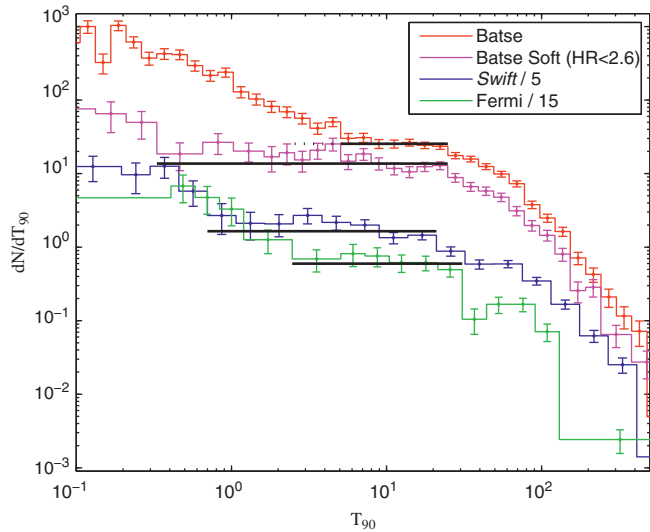


Figure 10.3 A plateau existing in the duration distribution of GRBs, giving direct evidence of jet propagation inside a massive star. Reproduced from Figure 1 in Bromberg et al. (2012) with permission. ©AAS.

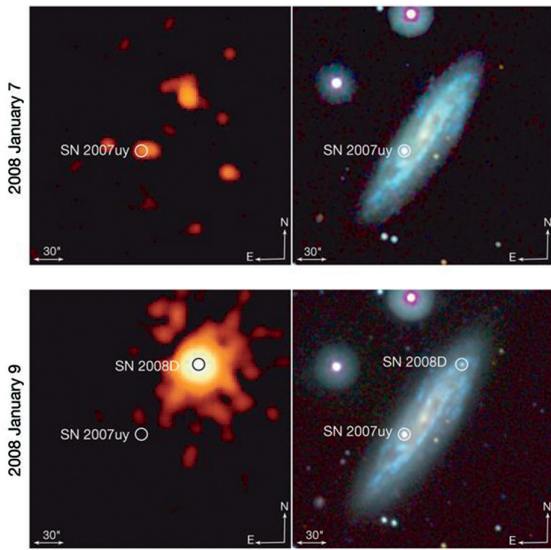


Figure 10.4 The discovery images of XRO 080109 and its associated supernova SN 2008D. From Soderberg et al. (2008).

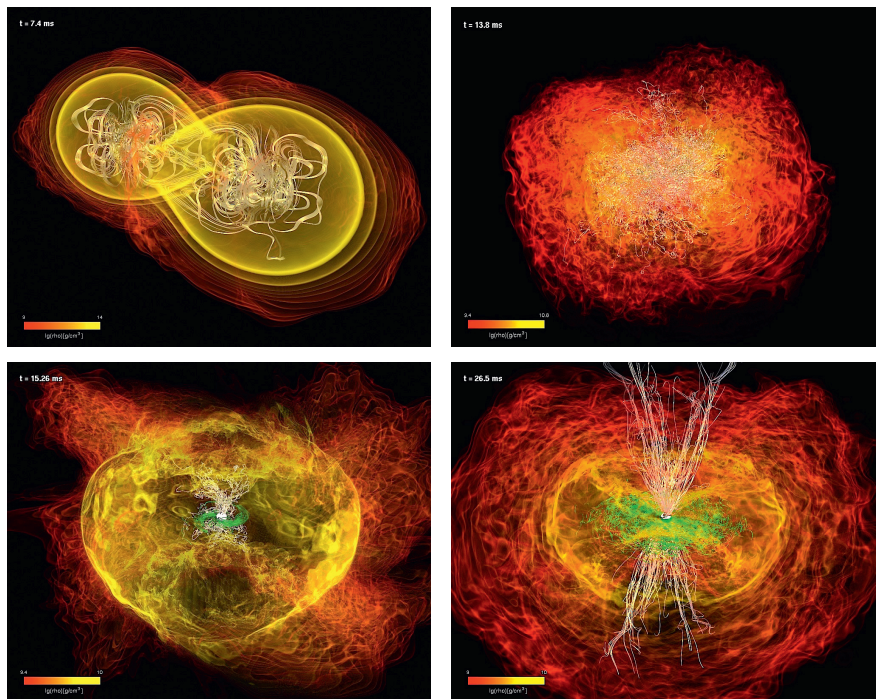


Figure 10.6 Numerical simulations that show launching of a broad outflow from NS–NS mergers. Four snapshot density images with magnetic field lines (green for within the torus and equatorial plane; white for outside the torus and near the BH spin axis) are shown. Reproduced from Figure 1 in Rezzolla et al. (2011) with permission. ©AAS.

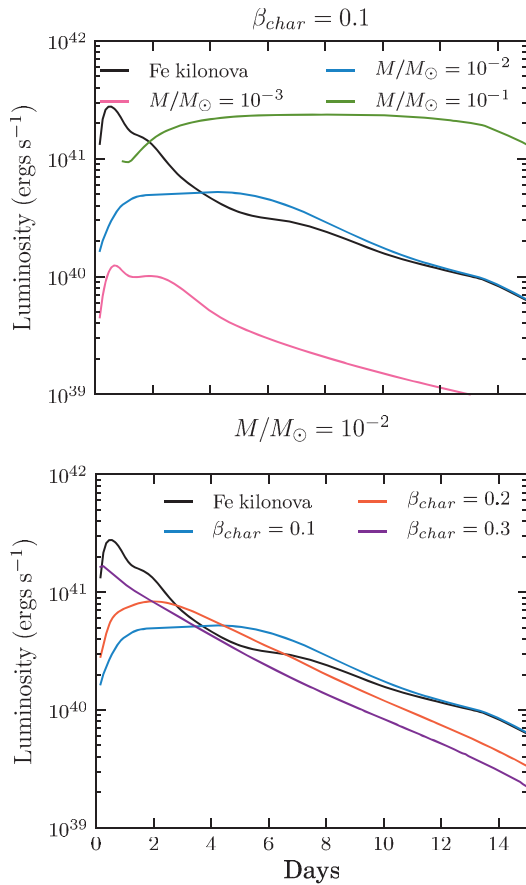


Figure 10.7 The kilonova bolometric lightcurves comparing the low- κ Fe ejecta and high- κ lanthanide ejecta. Reproduced from Figure 2 in Barnes and Kasen (2013) with permission. ©AAS.

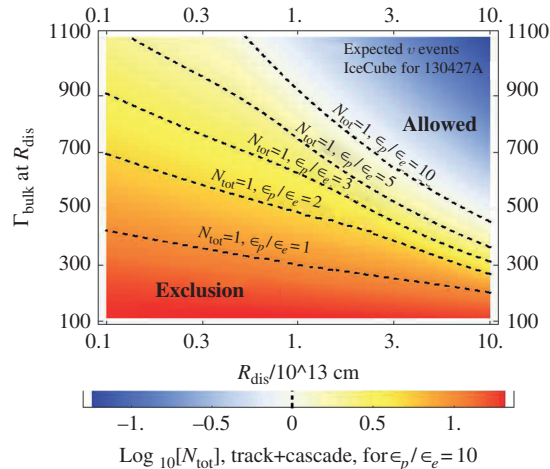


Figure 12.5 Constraints on the parameter space with the non-detection of neutrinos from GRB 130427A. Reproduced from Figure 1 in Gao et al. (2013d) with permission. ©AAS.

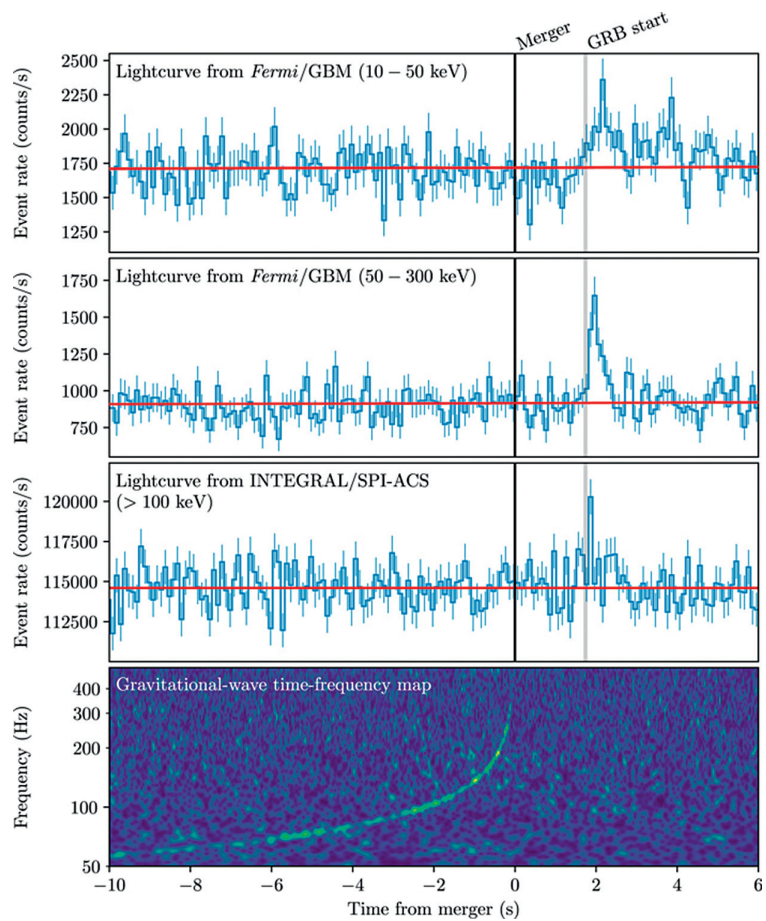


Figure 12.6 Joint, multi-messenger detection of GW170817 and GRB 170817A. Reproduced from Figure 2 in Abbott et al. (2017b) with permission. ©AAS.

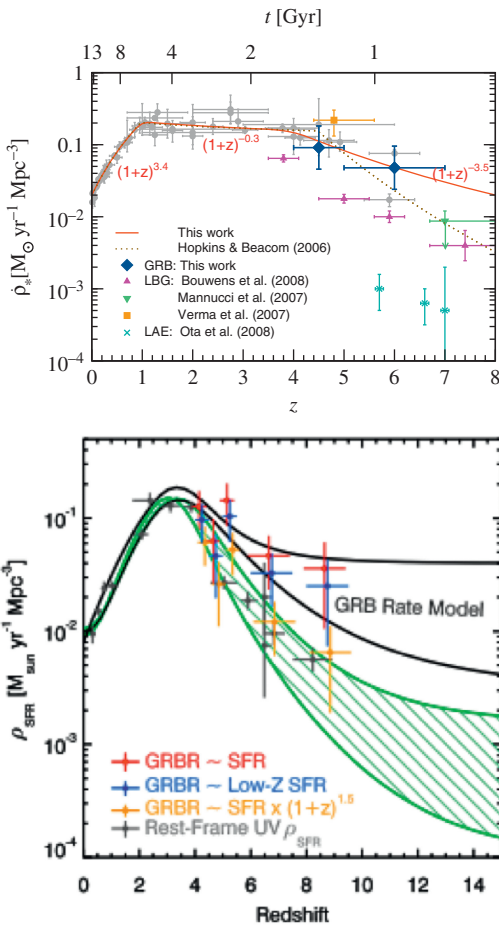


Figure 13.4 *Upper:* Star formation history measured with multiple observational probes and an analytical fit. Reproduced from Figure 1 in Yüksel et al. (2008) with permission. ©AAS. *Lower:* The SF rate probed with the rest-frame UV flux (lower solid crosses and the shaded region) and with GRBs (three different models). One can see that in any case GRBs probe a higher SF rate at high- z relative to the rest-frame UV flux, suggesting a high- z excess. Reproduced from Figure 5a in Robertson and Ellis (2012) with permission. ©AAS.

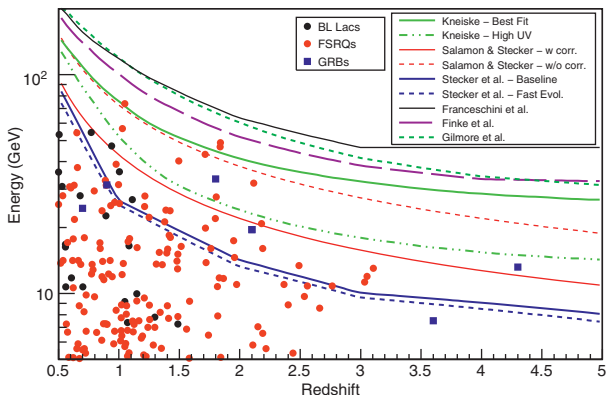


Figure 13.9 Highest energy photons from blazars and GRBs from different redshifts against the predictions of $\gamma\gamma$ optical depth $\tau_{\gamma\gamma} = 1$ for various EBL models. Some models (e.g. the “baseline” model of Stecker et al. 2006) have been ruled out by the data. (See Abdo et al. 2010 for references.) Reproduced from Figure 3 in Abdo et al. (2010) with permission. ©AAS.